

## TWO-DIMENSIONAL HIGH PRECISION THERMAL NEUTRON DETECTOR \*

R.A. BOIE, J. FISCHER, Y. INAGAKI, \*\* F.C. MERRITT, H. OKUNO \*\*\* and V. RADEKA  
*Brookhaven National Laboratory, Upton, New York 11973, U.S.A.*

Received 12 January 1982

A position resolution of 1.3 mm (fwhm) and integral non-linearity of  $\pm 0.1\%$  is achieved in a two-dimensional  $18 \times 18 \text{ cm}^2$  thermal neutron detector. The gas proportional detector operates at a moderate pressure (5–6 atm) with a  $^3\text{He}-\text{C}_3\text{H}_8$  mixture and at very low required avalanche gain ( $\sim 30$ ) by virtue of the high precision centroid finding position readout.

### 1. Introduction

Two-dimensional position sensitive detectors are being increasingly used in neutron diffraction experiments for determination of molecular and crystal structures in biology, solid state physics and polymer chemistry. Position sensitive detectors for neutrons in the wavelength range from  $1.8 \text{ \AA}$  ( $\sim 25 \text{ meV}$ , i.e., “thermal neutrons”) to about  $8 \text{ \AA}$  ( $\sim 1.2 \text{ meV}$ , i.e., “cold” neutrons) require a high detection efficiency for neutrons and a low efficiency for background  $\gamma$ -rays, high uniformity of efficiency, good position resolution at counting rates of up to  $10^5 \text{ s}^{-1}$ , high position accuracy, little scattering in the entrance window, and stable maintenance free operation over long periods of time.

Detectors built at BNL according to the original development reported previously [1] have been operated successfully as part of facilities for biological research at the High Flux Beam Reactor.

Recently, we have made some substantial improvements in all of the detector characteristics listed above. The advances which have made this possible are in two areas: (1) a new method has been developed for position sensing, and (2) new gas mixtures have been explored, allowing higher position accuracy and resolution at lower gas pressures. A new detector based on these advances is described in this paper.

Some basic considerations in the design of two-dimensional neutron detectors are given in ref. 1, where the choice of the neutron induced reaction and the detection method are discussed.

For quantitative neutron diffraction experiments, where position accuracy, uniformity of efficiency and stability of response are of utmost importance, gas proportional detector – properly applied – are the most suitable so far. Our neutron detectors are based on the ionization produced by the charged-particles from the reaction  $^3\text{He} + n \rightarrow ^3\text{H} + p + 0.764 \text{ MeV}$ . Some alternative approaches are described in refs. 5, 6 and 7.

A principal problem of gas detectors, combined with conventional position readout methods, is that the high avalanche size (usually in the one picocoulomb range) required for good position resolution results in impairment of several important detector characteristics. As the gas gain and the avalanche size are increased, the space charge thus created causes a nonlinear energy response. This results in poor energy resolution and an overlap between amplitude distributions for gamma rays and neutrons, which precludes their separation. Furthermore, at high gas gains the nonuniformity of the gas gain over the detector area increases (for a given non-uniformity of parameters of the detector electrode geometry). This and the poor energy resolution make the attainment of a high uniformity of efficiency and of stable operation difficult.

We have resolved this problem by development of a much more sensitive position readout method which allows a much lower avalanche size – in the range of less than one tenth of a picocoulomb. With a total energy of  $764 \text{ keV}$  of the proton and triton released in the neutron induced reaction, the primary ionization in gas is  $\sim 3 \times 10^4$  ion pairs. The readout requires a gas gain of only about 20–30, where the adverse effects of charge multiplication and the space charge are negligible.

We have reported the high precision position sensing method previously [2]. The principle of this method is illustrated in fig. 1. In this method the centroid of charge induced on the position sensing electrode is determined by convolution of the sequentially switched

\* This research was supported by the U.S. Department of Energy: Contract No. DE-AC02-76CH00016.

\*\* On leave from Kyoto University, Kyoto, Japan.

\*\*\* Present address: Institute for Nuclear Study, University of Tokyo, Tanashi, Tokyo, Japan.

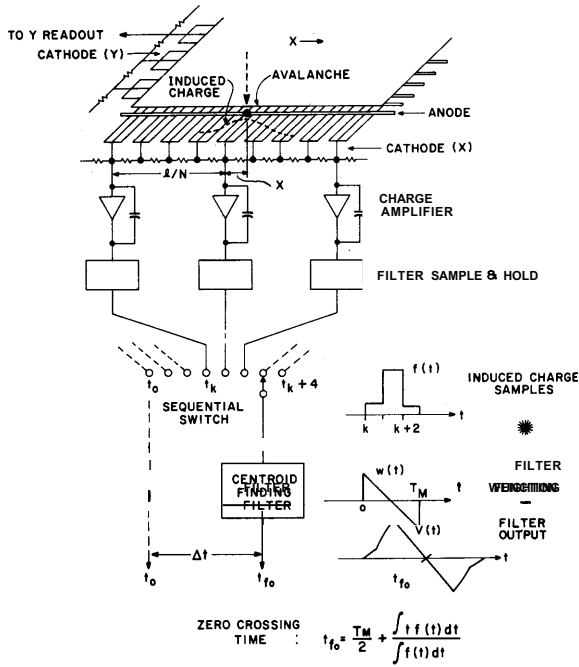


Fig. 1. Principle of the centroid finding method by convolution. Readout grids (marked as "cathode x" and "cathode y") are connected to their resistance chains. Preamplifier outputs from the subdivided resistance chain are switched sequentially into the centroid finding filter. Zero crossing time  $t_{fo}$  is a continuous linear function of the position  $x$  (or  $y$ ) of the induced charge over the whole detector. Noise from only three outputs affects the result of this measurement.

outputs from a subdivided resistance chain with a linear centroid finding filter. The method achieves a high absolute position accuracy and a high position resolution with small avalanche charge by virtue of a number of signal outputs from the detector, i.e., by the subdivision of the detector. Yet this readout provides an output which is a continuous linear function of the position over the whole detector. The readout system for this detector is described in some detail in ref. 3.

The electrode geometry of the detector is illustrated in fig. 2. There are two orthogonal readout grid planes between the anode plane and the cathode planes. These grids are connected to the position readout as shown in fig. 1. Neutrons enter the chamber through an aluminum window, which has to be of sufficient strength to withstand the gas pressure. The energetic reaction products (proton, 573 keV, and triton, 191 keV) are emitted in opposite directions. We measure the centroid of the ionization produced. Due to the large difference in energy and range of the proton and the triton, the ionization centroid is displaced from the interaction point. This is a fundamental limitation to the measurement resolution. The position resolution limit is thus determined by – besides the electronic noise in the position readout – the stopping power of the gas for the charged particles.

It is obvious that the gas filling has to satisfy a difficult set of requirements: (1) high detection efficiency for neutrons; (2) high stopping power for charged particles; (3) low conversion efficiency for

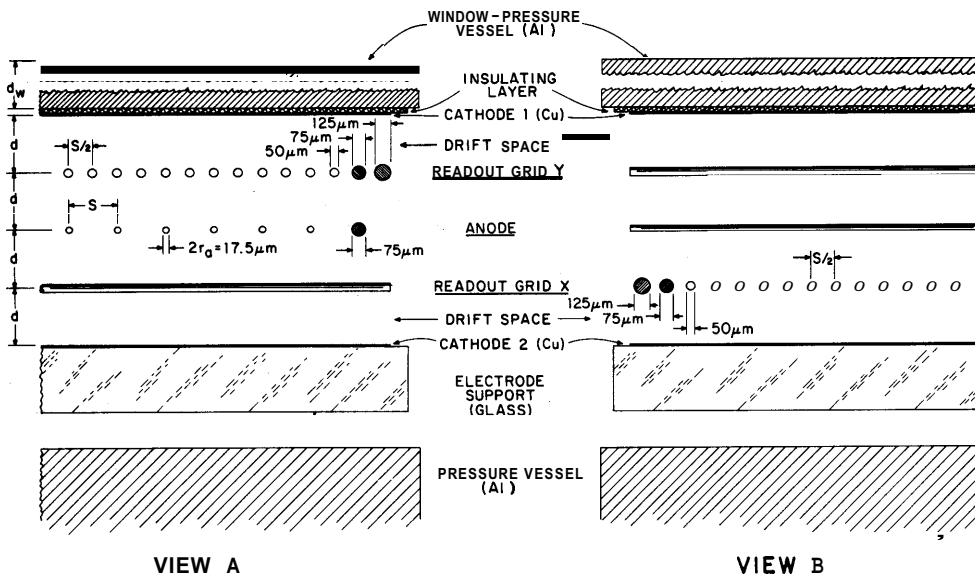


Fig. 2. Schematic representation of the electrode geometry of the 18X 18 cm<sup>2</sup> two-dimensional position sensitive detector. Spacing between adjacent electrode planes is  $d = 3.6$  mm; thickness of the active region is  $4d = 14.4$  mm; anode wire pitch is  $s = 2.54$  mm; readout grid pitch is  $s/2 = 1.27$  mm. Thickness of the aluminum window for a total pressure of 10 atm is  $d_w \approx 9$  mm.

gamma rays; (4) good properties for charge amplification; (5) it must satisfy (1) and (2) at a low overall pressure; and (6) it must be suitable for circulating purification. A study of gases has resulted in a  $^3\text{He}$ - $\text{C}_3\text{H}_8$  mixture, which is compatible with these requirements. This gas mixture should also be operated at a low avalanche charge in order to reduce organic molecule decomposition and formation of deposits on electrodes. This is consistent with the centroid finding position readout. These two steps combined result in significantly better position sensitive neutron detectors.

On an  $18 \times 18 \text{ cm}^2$  detector, a position resolution of 1.3 mm (fwhm) has been achieved at a total gas pressure of 6 atm, and with an absolute position accuracy of better than 1 part in  $10^3$ .

The choice of gases is discussed in section 2. The electrode geometry and the detector construction are described in section 3 and in figs. 2–4. The circulating gas purifier is described in section 4 and in fig. 5. Position readout and noise limited resolution are discussed in section 5 and in figs. 1, 6 and 7. The position resolution function, due to a long range of charged particles, is discussed with the resolution measurement results in section 6 and in figs. 8 and 9. Position accuracy considerations and measurement results are given in section 7 and in figs. 10 and 11. The centroid finding filter is described in the appendix and in figs. 12 and 13.

## 2. Choice of gases

$^3\text{He}$  is the most suitable neutron sensitive ingredient of the gas filling. Its favorable properties are a high neutron cross section, chemical inertness, and good behavior in proportional detectors at high pressures. The  $^3\text{He}$  pressure and the detection medium thickness are usually selected for a neutron detection efficiency of 60–90%, depending on the neutron wavelength. A wavelength range of interest in diffraction experiments is between 1.82 Å and 8 Å. The cross section for neutrons at 1.82 Å is  $\sim 5330 \text{ b}$  and at 8 Å it is  $\sim 2.4 \times 10^4 \text{ b}$ . One to six atmospheres of  $^3\text{He}$  are usually required with an active thickness of the detector of 1–1.5 cm. The disadvantage of  $^3\text{He}$  are its cost, and its high rate of diffusion through certain materials. The former makes a closed gas system mandatory, and the latter requires attention to the design of a very tight detector enclosure.

$^3\text{He}$  by itself is not sufficiently dense at reasonable working pressures to stop the proton and the triton from the  $^3\text{He}(\text{n}, \text{p})^3\text{H}$  reaction within a distance short enough for good position resolution. Thus another ingredient is needed in the gas mixture whose function is to stop the charged particles from the nuclear reaction. Argon has been commonly used in  $^3\text{He}$  detectors, as well as in some of our previous detectors. With about

4 atm of argon, the position resolution is limited by the range of the charged particles to about 2 mm (fwhm). Stable operation of the detector in the proportional amplification mode requires a quenching gas.  $\text{CO}_2$  or  $\text{CH}_4$  at 5–10% of the total pressure of the mixture have been the most common gases used.  $\text{CO}_2$  is not convenient for a closed gas mixture, since it is absorbed by the purifier. These mixtures (typically 4–6 atm  $^3\text{He}$  + 4 atm Ar + 0.5–1 atm  $\text{CH}_4$ ), while having been used successfully, require high gas pressures to achieve good position resolution. In particular, at a total pressure of 10 atm, frequently needed with argon–helium mixtures, the design of gas enclosures for larger detectors becomes very difficult.

As a result of a study of various gases to reduce the charged particle range, to reduce the gamma ray conversion efficiency, and to reduce gas pressure, argon was replaced by propane ( $\text{C}_3\text{H}_8$ ). Propane is about 2.7 times more effective in reducing the charged particle range. In this case, propane at 1.5 atm is equivalent to argon at 4 atm. This results in a lower gas pressure at equal position resolution. With a moderate increase in pressure – still below the argon pressure – an even better position resolution is achieved, as will be shown in section 6. Propane also acts as its own quencher, and it is compatible with the purifier. It has a lower  $Z$  than argon, and thus its efficiency for gamma rays is lower.

The relation of the propane pressure and the position resolution is discussed in section 6. An approximate relation useful for design purposes can be described as,

$$\text{fwhm} \times p(\text{C}_3\text{H}_8) \approx 3 \text{ mm atm.} \quad (1)$$

As the pressure of propane is increased, the maximum avalanche charge before the onset of degradation in energy resolution decreases. The required detector voltage increases.

The upper limit for the avalanche charge is determined by the energy resolution required. Amplitude spectra for neutrons and gamma rays as a function of avalanche charge for 2.5 atm of propane are given in fig. 6. For an adequate separation of neutrons from a gamma ray background, the avalanche charge (measured in  $1 \mu\text{s}$ ) should not exceed  $(5\text{--}6) \times 10^5$  electrons for this gas mixture.

Thus this gas mixture has only two components,  $^3\text{He}$  and  $\text{C}_3\text{H}_8$ . Their partial pressures can be determined independently on the basis of the neutron wavelength and the detection efficiency for  $^3\text{He}$ , and of the position resolution for  $\text{C}_3\text{H}_8$ . For example, a mixture of 4 atm  $^3\text{He}$  + 1.5 atm  $\text{C}_3\text{H}_8$  (total pressure 5.5 atm) in the detector with an active thickness of 14.4 mm will have an efficiency of  $\sim 85\%$  for 4 Å neutrons, and a position resolution  $\text{fwhm} \leq 2 \text{ mm}$ .

In our studies of the properties of heavy gases (e.g., position resolution vs propane pressure) and for initial

detector tests after their construction is completed, we have used temporary (expendable) gas mixtures where most of  $^3\text{He}$  is replaced by  $^4\text{He}$  (which has identical properties as a proportional detector gas), and a small amount of  $^3\text{He}$  provides the sensitivity for neutrons needed for the tests.

### 3. Electrode geometry and detector construction

The electrode geometry of the detector is illustrated in fig. 2. It consists of two wire grid planes for position readout of induced charges, centered between the anode and each cathode. The readout grids are oriented one parallel (grid *Y*) and one orthogonal (grid *X*) to the anode wires. The readout grids are at ground potential, in order to avoid the necessity for high voltage coupling capacitors to preamplifiers. Consequently, the anode plane is at a positive high voltage and the cathodes are at a negative high voltage. The electric field in the cathode-grid drift spaces is somewhat lower than in the grid anode spaces in order to avoid collection of electrons from primary ionization on the readout grids. All electrode planes are terminated at their boundaries with wires of larger diameters to avoid increased electric field at the end wires which would cause electric discharge. The anode plane wires are all connected together to obtain the total energy signal, which is used for neutron discrimination and for gating of the position readout. The readout grid wires are attached to printed circuit boards and interconnected with resistors in groups of two. The taps on these two resistance chains are brought out of the detector enclosure and connected to the preamplifier. The electrode structure is shown in photographs, figs. 4a, b, and c.

The electrode planes are built up on a flat glass plate 6.4 mm thick, which is covered with evaporated copper serving as cathode 2. Grid *X* first, the anode wires second, and then grid *Y*, are laid on fiberglass (G10) bars of appropriate thickness each having a printed circuit top. The distance to the front cathode, i.e., the window, is set by the spacer plugs. The entire electrode assembly is pressed against the window-pressure vessel by four springs located beneath the glass plate, while its lateral position is maintained by guide bars.

The whole detector is shown in fig. 3. The circulating pump, gas purifier, pressure indicator, safety relief, filling valves and signal processing electronics are mounted on the rear of the plate supporting the detector enclosure. The enclosure consists of a thick base plate (30 mm) which carries the electrode structure, as shown in fig. 4a, and of a front cover which contains the window and cathode 1 as shown in fig. 4c. The enclosure is designed for a working pressure of 8 atm, and is made of 6061T6 aluminum. The two parts of the enclosure are held together by hardened steel bolts. The seal between

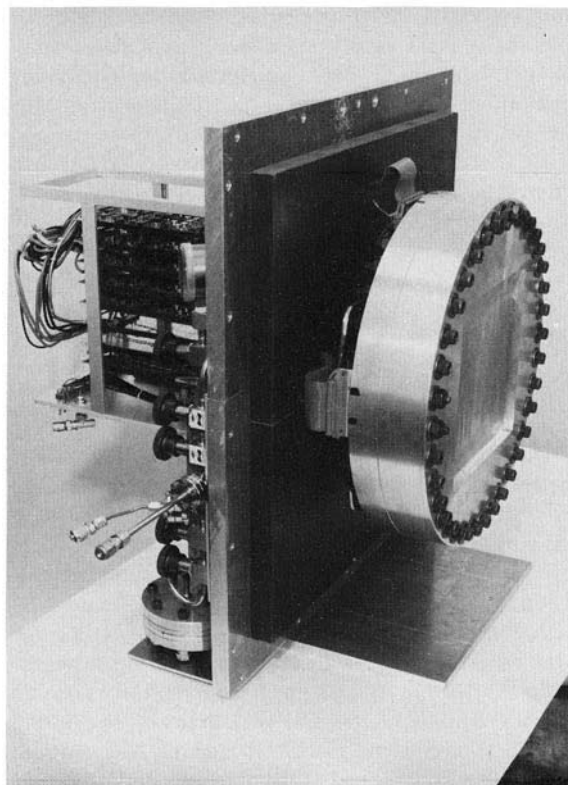


Fig. 3. Two-dimensional high precision detector for thermal neutrons with an active area of  $18 \times 18 \text{ cm}^2$ . Most of the electronics for the centroid finding position readout is on the rear side of the detector. Gas purification system is also shown in this figure. (Between the detector pressure vessel and the electronics is a part of the neutron shielding.)

the two parts is by means of two concentric helium resistant O-rings, fig. 4c. All electric and gas feedthroughs are doubly sealed. They are sealed individually on the inside of the base plate by a low vapor pressure epoxy, and on the outside by an O-ring for each group of 8 pins for electrical connections. This provides a sufficiently tight enclosure so that no significant decrease in pressure due to helium leakage was observed after one year.

The front cover has a square recess of  $20 \times 20 \text{ cm}^2$  on the outside to provide a 9mm thick window for the neutrons. Since the interior of the window serves as a base for the front cathode (1), it has to be flat to within about one percent of the anode-cathode spacing ( $\leq 70 \mu\text{m}$ ). Larger deformation would result in noticeable nonuniformities of the detection efficiency and the gas gain. The window deflects by about 0.2 to 0.3 mm in the center under gas pressure of 8 atm. The inner window surface was machined while under a similar load applied mechanically, in order to achieve the required

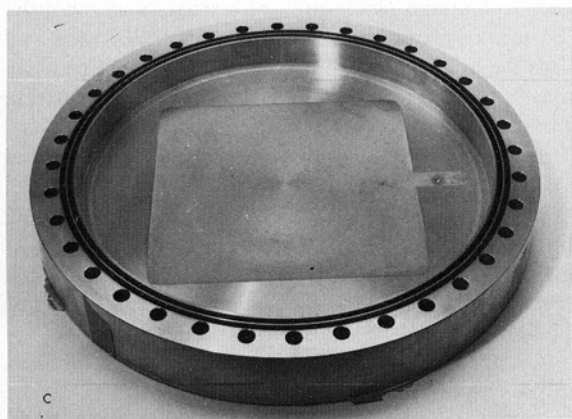
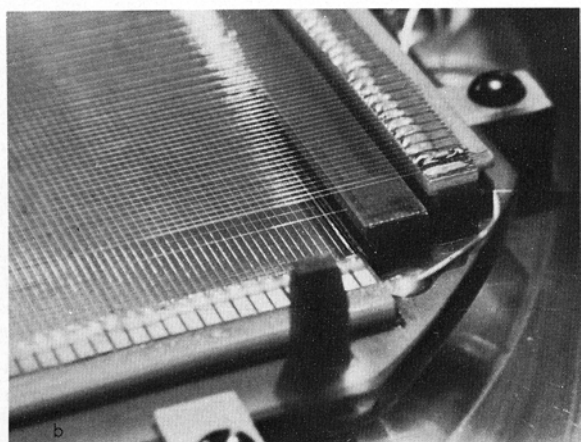
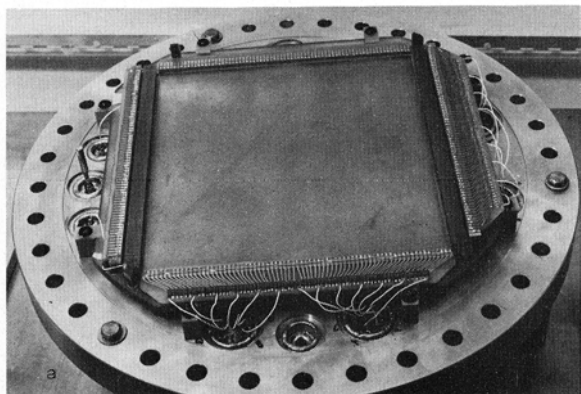


Fig. 4. Electrode system of the detector shown in fig. 3. (a) Anode and grid wire planes. Resistive chain is visible for the readout grid. Connection leads from subdivision nodes on the resistance chain (fiducial points) to feedthrough connections can be seen for both coordinates. (b) Detail of the anode and the two readout grid wire planes and their supports. (c) Window-pressure vessel cover with insulated cathode 1.

flatness under pressure. Cathode 1 was then made by coating the window with a  $60\text{ }\mu\text{m}$  thick flexible insulating layer of Parylene C (made by Union Carbide Corp.) and by evaporating a copper electrode on it ( $\sim 1\text{ }\mu\text{m}$  thick). (This is an example of the window design for the maximum gas pressure anticipated.)

The window thickness of 9 mm results in some neutron scattering (about 7% at  $2.2\text{ }\text{\AA}$ , for example). The required gas pressure and the window design is determined by the neutron wavelength and detection efficiency (partial pressure of  $^3\text{He}$ ) and by the position resolution (partial pressure of  $\text{C}_3\text{H}_8$ ).

#### 4. The circulating gas purifier

The high price of  $^3\text{He}$  (over \$150 per liter) implies a closed gas preserving system. The gas circulating purification system (see figs. 3 and 5) consists of a container with a filter and absorber material which can be regenerated and a bellows pump, all operating at the detector gas pressure.

The purifier permits wide choice of chamber construction materials not normally allowed in a "clean" chamber. In this case G10 or FR5 fiberglass, printed circuit boards, as well as a number of metal film resistors in the resistance chain for position readout were included without adverse outgassing effects during 14 months in this detector and for several years in others. The purifier also has to remove the normal gas contaminants like water vapor, oxygen, and other electronegative impurities. During the operation the decomposition products of the organic gas and the polymerization products, caused by the avalanche, should be removed to minimize deposits on the electrodes and to ensure the stability of operation. While a higher rate of deposit formation should be expected with propane mixtures than with argon mixtures, the much lower avalanche charge and the very low gas gain used here should keep this rate low.

The purifier, which can be reactivated, consists of a stainless steel cylinder filled for one half of its length with "Ridox" (Fisher Scientific Co., Fair Lawn, NJ 07410) which acts mainly as an oxygen absorber. The other half is filled with a molecular sieve material, e.g., pore size  $3\text{ }\text{\AA}$ , mainly for water absorption. The molecular sieve also traps some polar and other molecules. Mechanical filters close the cylinder at each end. The purifier is activated with a mixture of argon +5%  $\text{H}_2$ , while at  $200^\circ\text{C}$  for a few hours, and subsequently pumped out. Several years of operation are estimated before reactivation is required.

The choice of chamber gases is also limited by the purifier materials since permanent poisoning of the purifier, or excessive absorption of the working gas is undesirable. In the case of the mixtures  $^3\text{He} + \text{argon} +$

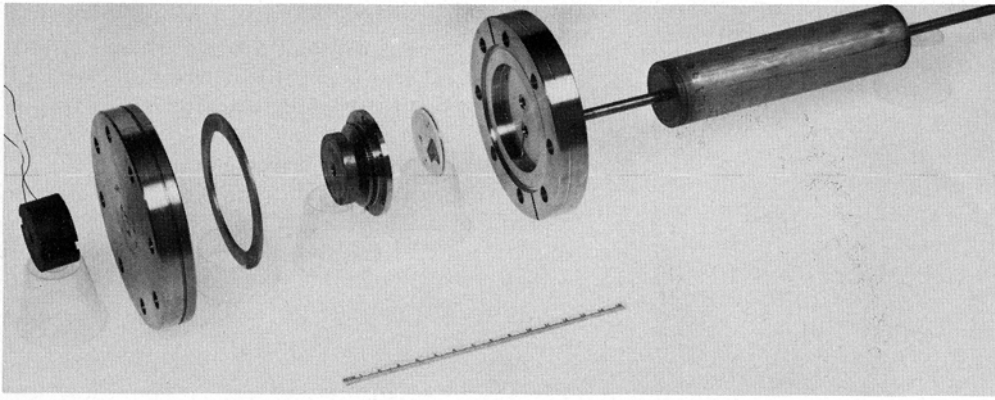


Fig. 5. Gas circulating pump. The main components of the pump are (from left to right): ferrite core electromagnetic drive, flange, gasket, bellows and soft iron disk with a resonance frequency of 60 Hz, reed valve plate, flange and the purifier container.

methane, which we used previously, there was negligible methane absorption. In the present case of  $^3\text{He} + \text{C}_3\text{H}_8$ , the absorption and release of the propane is significant and the equilibrium is temperature-dependent. In the interest of stability of the gas gain during experiments, it is advisable to maintain the detector temperature within  $\pm 5^\circ\text{C}$ .

The circulating pump, fig. 5, is enclosed by a pair of stainless steel Varian flanges (diameter 11.4 cm). One flange which carries the intake and outlet tubes has a small slot inside to connect the incoming gas to the volume between the two flanges. Attached to this flange is a reed valve plate with Teflon gaskets inside stainless steel bellows (both obtained from Metal Bellows Co., Sharon, MA 02067). The original bellows part was modified and provided with a screw connection to a soft iron disk, 50.8 mm in diameter. The thickness of the disk is adjusted to about 6.3 mm so that it resonates with the bellows at 60 Hz. The other enclosing flange is hollowed out to a thickness of 1.5 mm. It accommodates the end of the bellows and the iron disk and leaves a free distance for an amplitude of oscillation of 1.5 mm. The pump is driven through the thin part of the flange by an external electromagnet supplied by 6.3 V at 60 Hz through a half-wave rectifier. The pumping speed is 1–2 l/min and it takes about 2 min for one cycle of gas through the detector volume.

## 5. Position readout and noise limited resolution

Fig. 1 illustrates the readout method. A brief summary of the method is as follows. The anode plane of wires is centered between two orthogonal position readout grid planes of wires. The grid wires are shown in this illustration connected in groups of three, forming in effect strips. The strips are interconnected by a chain of resistors. Low input resistance amplifiers are con-

nected to the resistance chain at intervals determined by signal and noise considerations, thereby subdividing the readout grid plane. Electronics for each subdivision consists of a charge sensitive preamplifier, followed by a time variant filter. Sample and hold circuits provide a stored measure of induced charge on each subdivision. The subdivision samples are sequentially switched into a centroid finding filter. The filter provides an accurate centroid measure, here a zero crossing time. This filter has the desirable property of including signals and noise only from subdivisions containing centroid information and thereby minimizes the line width broadening due to electronic noise. The line width varies with the number of subdivisions as  $1/N^{3/2}$ . The weighting function and the signal response of the filter are shown in the figure. The switching sequence and digital timers for each axis share a common clock and are started synchronously. The zero crossing from the centroid filter of each axis stops the timers. When one, and only one, zero crossing in each axis is detected the digital position information is transferred into the data collection system.

This method is described fully in ref. 2. The signal processing and the position readout electronics are described in ref. 3, and further details on the centroid finding filter are given in the appendix of this paper. In this section we discuss the position resolution limit due to electronic noise, and we determine the number of subdivisions and the signal processing time.

An appropriate relationship for the noise limited position resolution has been described and verified by measurements using a detector simulator [2,3]. The relationship is given by

$$\text{fwhm} = 3.35(a_{F2} \cdot a_{ef})^{1/2}(kTC_D)^{1/2} \times (\tau_F/\tau_{DS})^{1/2} \frac{l}{N^{3/2}} \cdot \frac{1}{Q_s}, \quad (2)$$

where  $a_{F2}$  is the form factor for parallel noise of the charge measurement filter,  $a_{\text{sub}}$  is the combined form factor for the subdivision method and the centroid finding filter,  $k$  is Boltzmann's constant,  $T$  is the absolute temperature,  $\tau_F$  is the charge measurement (filter shaping) time,  $\tau_{DS}$  is the time constant for one section of the subdivided diffusive RC line (comprised of the readout grid capacitance and the resistance chain),  $l$  is the detector length,  $N$  is the number of subdivisions and  $Q$  is the charge induced on the readout grid measured in time  $\tau_F$ . A detailed analysis of the position resolution in centroid measurements is presented in ref. 4.

Referring to measured amplitude distributions for neutrons and gamma rays (fig. 6), we note that for stable, long-term operation with good neutron-gamma discrimination and uniform detection efficiency, while

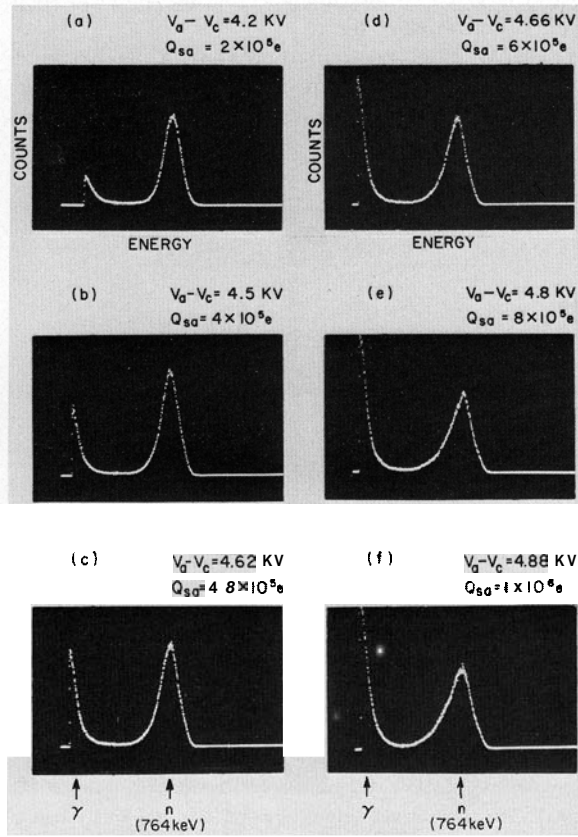


Fig. 6. Amplitude spectra for neutrons and gamma rays as a function of the avalanche charge. The peak is due to thermal neutrons (i.e., the resulting proton and triton pairs), and the low energy portion of the spectrum is due to gamma rays. The separation between neutrons and gamma rays decreases with increasing avalanche charge. The gas mixture is  $^3\text{He}$ (0.5 atm)  $^4\text{He}$ (2.5 atm) and  $\text{C}_3\text{H}_8$ (2.5 atm). The avalanche charge is measured in  $1\text{ps}$ .  $V_a - V_c$  is the potential difference between the anode and the cathodes 1 and 2 in fig. 2.

allowing some gas gain variation, an upper limit for the avalanche charge of about  $6 \times 10^5 \text{e}$  (in  $1\text{ps}$ ) is appropriate. Approximately 40% of this charge is available on each readout grid. The readout grid capacitance,  $C_D$ , is  $\approx 150\text{pF}$  and the length of the detector is 183 mm in each direction. The noise limited resolution chosen to be consistent with the limit due to the displacement of the ionization centroid is  $\leq 1\text{mm}$  (fwhm) for the  $X$  direction. Because of the further limit imposed by the quantization of position information in the  $Y$  direction, due to the anode spacing, a limit of  $\leq 2\text{mm}$  (fwhm) was chosen for the  $Y$  direction.

The filter form factors  $a_{F2}$  and  $a_{\text{sub}}$  are approximately 1.0 and 4.3, respectively. The ratio  $\tau_F/\tau_{DS}$  should be  $\approx 0.8$  for an impulse signal from the detector [2]. Using these parameters, nine subdivisions are required for the  $X$  direction and five subdivisions are required in the  $Y$  direction. We chose twelve and eight subdivisions ( $N_x = 12$  and  $N_y = 8$ ), which allows for a larger value of the ratio  $\tau_F/\tau_{DS}$  required for a long charge collection time, and provides convenient grouping of wires and resistors within the subdivisions.

The choice of the time parameters  $\tau_F$  and  $\tau_{DS}$  is determined primarily by the charge collection time in the detector.  $\tau_F$  must be long enough to collect sufficient signal charge. The signal current is induced by the motion of positive ions from the avalanche region near the anode wire. This current is extended in time due to a low positive ion mobility in these high pressure gas mixtures. A time of 1 to  $2\mu\text{s}$  is required to observe about one half of the total avalanche charge, where the observed charge increases logarithmically with time. The time constant  $\tau_{DS}$  is determined by the detector (readout grid) capacitance per subdivision  $C_{DS} = C_D/N$  and the resistance  $R_{DS}$  of the chain between two adjacent nodes (signal outputs). Since the induced charge is increasing at the time of the (sampling) measurement, the division of charge on the RC line will not be complete and there will be an error in the measured position. This error decreases as the measurement time  $\tau_F$  is increased in relation to  $\tau_{DS}$ . However, the effect of electronic noise on the position resolution increases with  $\tau_F/\tau_{DS}$ , eq. (2). On the basis of measurements and calculations, we found a minimum value of  $\tau_F/\tau_{DS} \approx 1.7$  for this detector, which was used in all measurements reported here with the values  $\tau_{DS} = 1.4\mu\text{s}$  and  $\tau_F = 2.4\mu\text{s}$ .

Fig. 1 indicates grouping of readout grid wires into strips which is done simply to minimize the number of resistors in the chain. The condition for the maximum pitch  $w$  of readout strips is  $\leq 0.8d$ , where  $d$  is the spacing between the anode readout planes, in order to ensure a linear relation between the centroid determined by the linear centroid finding filter from the samples of charge induced on the strips and the true position [2,3]. To satisfy this condition, readout grid wires are con-

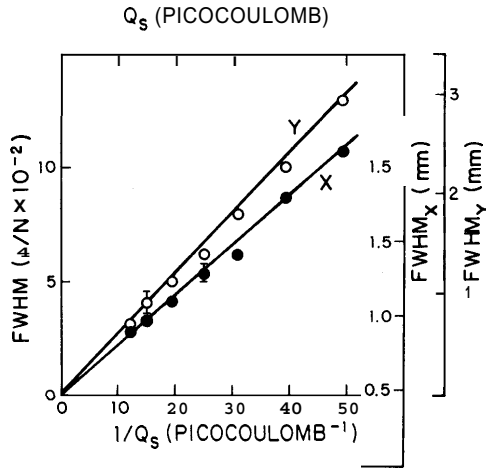


Fig. 7. Position resolution due to electronic noise as a function of the charge on the readout grids (the avalanche charge is  $-2.5$  times larger).  $l$  is the length of the readout and  $N$  is the number of readout subdivisions. For this detector  $l_x = l_y = 182.88$  mm. In the fine resolution axis the number of readout subdivisions  $N_x = 12$ , and the length of the readout section is  $l_x/N_8 d_x = 15.24$  mm. In the coarse resolution axis  $N_y = 8$ , and  $l_y/N_y = 22.86$  mm. Solid lines represent the position resolution calculated from eq. (2), and the circles  $\bullet$  and  $\circ$  are the measurement results for x and y axis, respectively.

nected to the resistance chain in groups of two, giving  $w/d = s/d = 2 \times 1.27 \text{ mm}/3.6 \text{ mm} = 0.71$ .

Thus we have the following principal parameters of the position readout, in this case: the number of subdivisions  $N_x = 12$ ,  $N_y = 8$ ; dimensions of the detector active area are  $l_x = l_y = 182.88$  mm; the length of the readout sections, i.e., the spacing between the nodes (outputs)  $l_x/N_x = 15.24$  mm,  $l_y/N_y = 22.86$  mm; the total number of readout grid wires for grid X is  $(6 \times 2 \times N_x + 1) = 145$  and for grid Y it is  $(9 \times 2 \times N_y + 1) = 145$ ; the total number of anode wires is 72; the resistance chain subdivisions between the nodes are  $R_{DSx} = 6 \times 18 \text{ k}\Omega = 108 \text{ k}\Omega$  and  $R_{DSy} = 9 \times 8.2 \text{ k}\Omega = 73.8 \text{ k}\Omega$ .

The noise limited position resolution measured by injecting charge through test capacitors into the subdivision nodes of the detector and the readout system is presented in fig. 7. The solid lines represent calculated resolution for the two axis. Fwhm,  $\approx 1$  mm is achieved on the fine resolution axis at a charge induced in the readout grid of  $\sim 2 \times 10^5$  e, which corresponds to an anode avalanche charge of  $\sim 5 \times 10^5$  e in  $\tau_F = 2.4 \mu\text{s}$ .

## 6. Position resolution limit due to displacement of ionization centroid

The proton and triton products of the  $^3\text{He}(n, p)^3\text{H}$  reaction are emitted in opposite directions and the

emission is isotropic. Each particle produces a track of ionization. The electrons drift toward the region of the anode wires where an avalanche forms. The motion of the positive ions produced by the avalanche and moving away from the anode induces a charge distribution on the position readout grids. The position determined for each axis is a measure of the centroid of the distribution of the induced charge which, in turn, corresponds to the centroid of the projection of the ionization distribution on each axis. The centroid of the ionization is displaced with respect to the point of the nuclear reaction due to different energy and range of the proton and the triton.

The spatial distribution of ionization track centroids for a point illumination with a flux of thermal neutrons has the form of a spherical shell. Neglecting for the moment all broadening, i.e., assuming a thin shell, the probability distribution of centroids measured along one axis of the detector is a rectangular function whose width is given by the diameter of the spherical shell. This is illustrated in fig. 8.

The position spectrum shown in fig. 9a illustrates this flattened distribution. Here a 0.3 mm diameter beam of  $2.4 \text{ \AA}$  neutrons is incident normal to the detec-

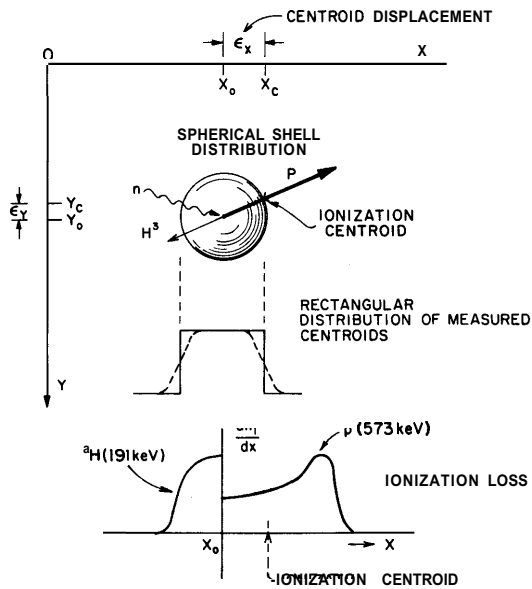


Fig. 8. The position resolution function due to a long range of the charged particles from the reaction  $^3\text{He} + n \rightarrow ^3\text{H} + p + 0.764 \text{ MeV}$ . The centroid of the ionization charge is displaced with respect to the point of the nuclear reaction due to different ionization loss of the proton and the triton. The loci of the centroids for many neutrons are uniformly distributed on the surface of the sphere. The resulting probability distribution in any one axis is a rectangular one. The effects of range straggling or of electronic noise in the position readout is indicated by dashed lines. The ionization loss curves for protons and tritons are shown only qualitatively.



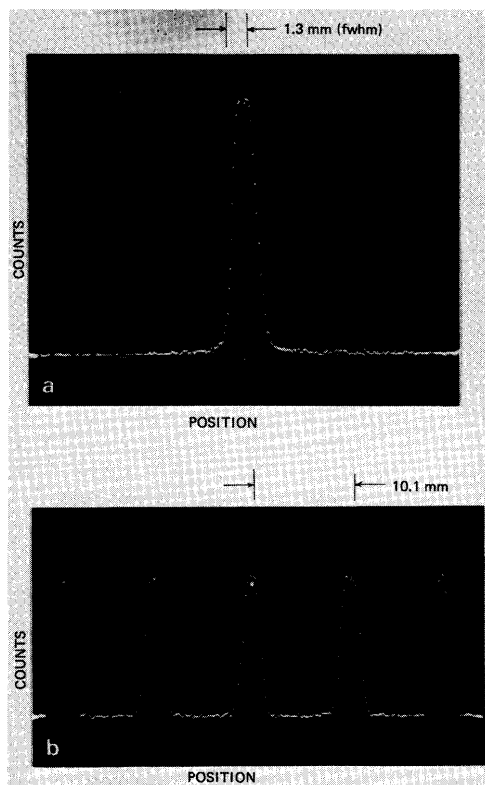


Fig. 9. Measured position resolution for 2.4 Å neutrons. (a) Gas mixture  $^3\text{He}(0.5 \text{ atm}) + ^4\text{He}(2.4 \text{ atm}) + \text{C}_3\text{H}_8(2.5 \text{ atm})$ . Fwhm = 1.3 mm. Flattening of the top of the peak is due to ionization charge centroid displacement (see fig. 8). (b) Gas mixture  $^3\text{He}(0.5 \text{ atm}) + ^4\text{He}(3.5 \text{ atm}) + \text{C}_3\text{H}_8(1.5 \text{ atm})$ . Fwhm = 1.9 mm. Neutron beam scan in steps of 10.1 mm.

tor plane. The spectrum is a one-dimensional measurement along the anode wire, in  $X$  direction, with no sorting in direction  $Y$ , normal to anode wires. The spectrum shown was obtained at an equivalent anode signal charge of  $9 \times 10^5$  electrons (in 1 ps). The electronic noise limited resolution (fwhm) of 0.55 mm does not obscure the flat top of the position resolution function. The total width of the response at half height is 1.3 mm. The measurement is in reasonable agreement with values for the first moment of the ionization track calculated from published stopping power data for the ranges of the proton and triton. As noted in section 2, propane ( $\text{C}_3\text{H}_8$ ) has a stopping power 2.7 times that of argon. The calculated range of the 573 keV proton in 2.5 atm of  $\text{C}_3\text{H}_8$  is  $\sim 1.8$  mm. The available data and calculations for ionization loss of tritons at energies below 191 keV are not consistent. The results in the literature for the range of the 191 keV triton are between 0.2 and 0.5 of the proton range. Fortunately, the effect of this large uncertainty on the centroid is small, since the triton has only one quarter of the total energy.

Furthermore, only a part of this energy results in ionization, while the rest is spent in nonionizing collisions due to the low energy of the triton. The centroid displacement for both particles is between 0.63 and 0.75 of the centroid for the proton ionization loss distribution alone which is better known. The first moment of the resulting ionization is displaced by about 0.6 mm from the reaction point in the direction of the proton emission, resulting in a 1.2 mm wide rectangular distribution on the measurement axis. It is easy to show that as long as the Gaussian broadening terms due to range straggling, gas gain fluctuations, and the electronic noise, have combined fwhm of less than half of the rectangular distribution width, the resultant width at one half-maximum is given only by the width of the rectangular distribution. A reduction in the broadening terms serves only to sharpen the edges and not to modify the width at half-height. The range straggling for 573 keV protons is a few percent and it has a negligible effect. The largest effect at lower avalanche charge is due to electronic noise.

Fig. 9b shows a spectrum obtained at a lower  $\text{C}_3\text{H}_8$  pressure of 1.5 atm, with 0.5 mm diameter beam of 2.4 Å neutrons positioned in 10.1 mm steps. The full width at half maximum of 1.9 mm in this case compares again favorably with the estimated position resolution function width of 2 mm.

## 7. Position accuracy

### 7.1. Integral nonlinearity

One of the virtues of this centroid finding readout method is the uncoupling of the magnitude of the absolute position error from the length of the detector. The subdivision nodes provide a set of mechanically defined fiducial points. Imperfections and misadjustments of the individual subdivision circuits can only have a localized effect on position measurements. Thus the absolute position error is independent of the detector length, and the integral nonlinearity (the absolute position error normalized to the detector length) is inversely proportional to the detector length. A measured integral nonlinearity of  $< \pm 0.1\%$  is achieved for the  $X$  direction for a mechanically scanned collimated beam of thermal neutrons over the entire detector length. This corresponds to an absolute position error of better than  $\pm 180$  pm. These measurements with a neutron beam are difficult, and it is possible that the accuracy of this detector is better. The position readout was proved to have an absolute error of less than  $\pm 80 \mu\text{m}$  [2,3]. The errors in the positioning of readout grid wires and anode wires are well within  $\pm 50$  pm. The stability of position calibration is inherent in this method of position readout. The level of accuracy achieved is better by

at least an order of magnitude than with other readout methods based on resistance electrodes or resistance chains.

## 7.2. Differential nonlinearity

Achieving a low differential nonlinearity is a more difficult matter. Differential nonlinearity is the derivative  $dx_m/dx$  of the position calibration curve  $x_m = f(x)$  where  $x_m$  is the measured position and  $x$  is the true position. Low differential nonlinearity is more or less important, depending on the neutron scattering patterns of interest. Patterns that are highly peaked have relaxed requirements compared to continuous spectra. A measure of differential nonlinearity is the departure from flat response of a uniform illumination spectrum. Of course, any nonuniformity of detection efficiency is also included in this spectrum.

This detector readout method was shown to be inherently continuous in nature with no discontinuities due to subdivision. The fiducial points provided by the subdivision boundaries assure that differential and integral nonlinearities are only localized effects. Linear response is achieved within subdivisions by equalizing the gain and offset of the nearby subdivision's signal processing channels. A gain misadjustment of a few percent will produce a localized differential nonlinearity of similar magnitude.

Fig. 10 shows a uniform illumination X direction spectrum obtained by thermal neutrons scattered from a vanadium target. There is no sorting in the Y direction for this data. We note the low error in the right half of

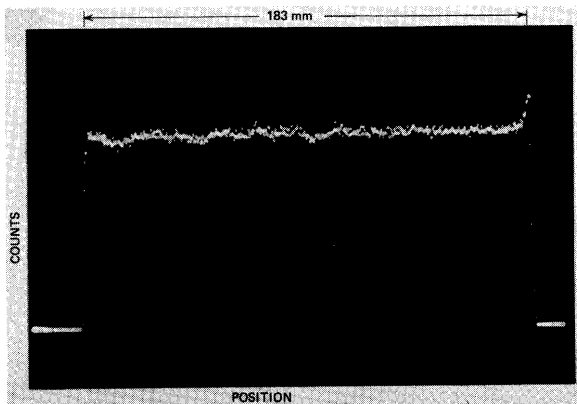


Fig. 10. Uniform illumination spectrum in the fine resolution axis (parallel to the anode wires) obtained by thermal neutrons scattered from a vanadium target. Differential nonlinearity is within  $\pm 3\%$ . The left part of the spectrum shows the effect of gain differences of individual readout channels from their mean value. The differential nonlinearity of the position readout system at any position is given approximately by the relative gain misalignment of the adjacent channels.

the spectrum where the gains are properly normalized, and a somewhat larger error in the left region, where the gain of corresponding channels is not yet aligned. Differential nonlinearity for this figure is  $\sim \pm 3\%$ .

## 7.3. Properties of position readout in the direction Y, orthogonal to anode wires

Fig. 11a is a photograph of a uniform illumination spectrum as seen in the Y direction. The modulation, shown more clearly by the expanded scale of fig. 11b, has the period of the anode wire spacing. The magnitude of the modulation is related to the ratio of the anode wire spacing to the total length of the ionization track produced by the proton and triton reaction products. Increasing the relative length of the ionization track (by reducing the gas pressure) will increase the sampling by the anode and thereby reduce the modulation. Increased *systematic* differential nonlinearity in the Y direction is the penalty for the improved position resolution in the X direction. [If the anode wire spacing is reduced, the induced charge Q, on the readout grids decreases, resulting in increased effect of the electronic noise, eq. (2). To counteract this, a larger number of subdivisions N would be necessary.]

The uniform illumination data shown were collected

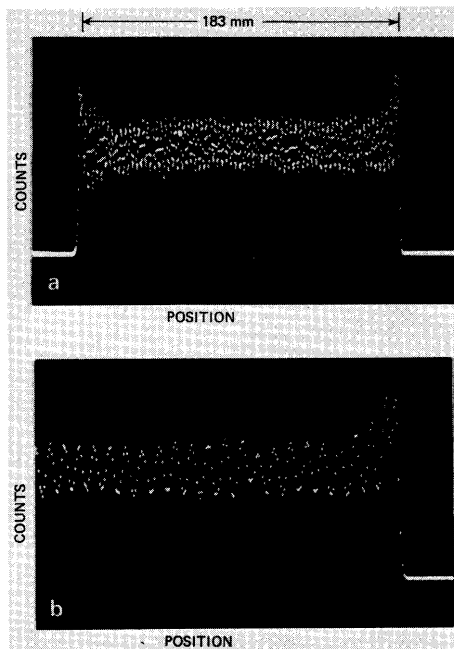


Fig. 11. Uniform illumination spectrum in the coarse resolution axis (perpendicular to the anode wires), shown for the whole detector (a) and on an expanded scale (b). The quantizing effect of the anode wires on the position information is apparent.

at high dispersion to illustrate better the structure in the spectra using a time-to-amplitude converter and a multichannel analyzer. The direct time-to-digital converters, which are a part of the readout system, were originally designed [3] to provide dispersions of exactly 512 position channels in the  $X$  direction and exactly 128 channels for  $Y$ . The performance of the timing circuits is adequate in terms of both integral and differential non-linearity. The numbers of channels selected should be consistent with the position resolution of the detector and with the requirements for minimum processing time and efficient organization of two-dimensional arrays in the memory space. However, there is another important aspect in the selection of the number of channels for the  $Y$  axis which we wish to emphasize here. The number of channels initially selected for the  $Y$  axis (128) is not an integral multiple of and not much larger than the number of anode wire spacings (72). This would result in a uniform illumination spectrum with an interference ("beating") effect between the periodic component of the detector position response in the  $Y$  direction and the (time) digitization of this response. Thus, it is essential in any such case to define the  $Y$  number of channels as an integral multiple of anode wire spacings. In the case of this detector, the maximum number of channels corresponding to the useful information provided in the direction orthogonal to anode wires is twice the number of anode wire spacings, i.e.  $2 \times 72 = 144$ .

A property of this readout system is that the position scale (in channels per unit length) is defined exactly by the spacing between the fiducial points (nodes on the resistance chain), and by the use of the same clock for both the sampling multiplexer and the time digitizer. The latter should also reduce the apparent modulation amplitude in the uniform illumination response.

The spacing (pitch) of readout grid wires is the same in both coordinates and it is equal to one half of the anode wire spacing. This, and the well-defined position scale provide rectangular picture elements with an integer aspect ratio.

The absolute position error in the  $Y$  direction at the minima and maxima of the uniform illumination response is as low as in the  $X$  direction along the whole axis.

## 8. Discussion

This paper describes some recent advances in the development of two-dimensional position sensitive detectors at BNL. The detector described, while developed specifically for certain experiments in solid state physics and biology, illustrates in its design a complex interdependence among the physical properties of the gas mixture, the electrode geometry and the position readout. The lower required avalanche charge offers a wider

range of possibilities in selection of gases and of electrode geometry, and it makes possible higher accuracy and stability of operation.

We wish to thank Dr. J.L. Alberi for many discussions on neutron detectors, and Drs. B.P. Schoenborn and S.M. Shapiro for many discussions on the development of appropriate detectors for experiments in biology and solid state physics, as well as for their support. Dr. R.P. DiNardo is gratefully acknowledged for development of coating techniques used in fabrication of the detector electrodes.

## Appendix

### Readout electronics

The input element of each subdivision signal processing circuit is a charge-sensitive preamplifier (with FET) with input resistance arranged to be less than  $200 \Omega$ . Two stages of gain, semi-Gaussian integration, a second order gated restorer and a sample and hold circuit complete the signal processing chain. The realized filter weighting function for the induced charge on each subdivision of the detector has the desirable bipolar trapezoidal form. At the measurement time,  $t_m$ , the

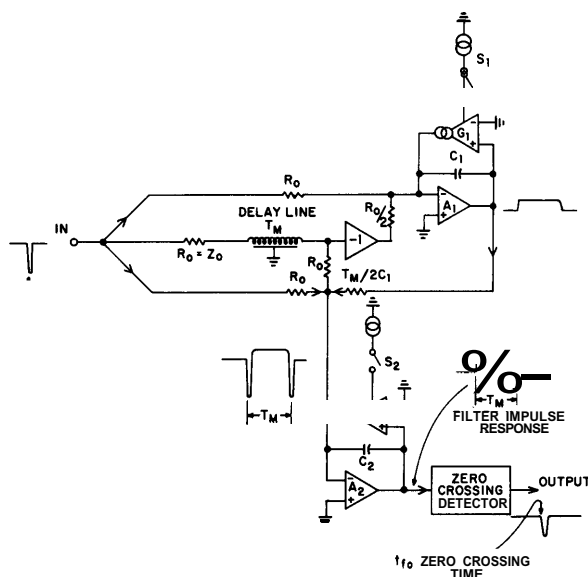


Fig. 12. Functional diagram of the centroid finding filter with response in Laplace domain

$$h(s) = \frac{2}{s} \left[ 1 + e^{-sT_m} - \frac{2}{T_m} \frac{1}{s} (1 - e^{-sT_m}) \right].$$

Filter impulse response is shown at the input to the zero crossing detector.

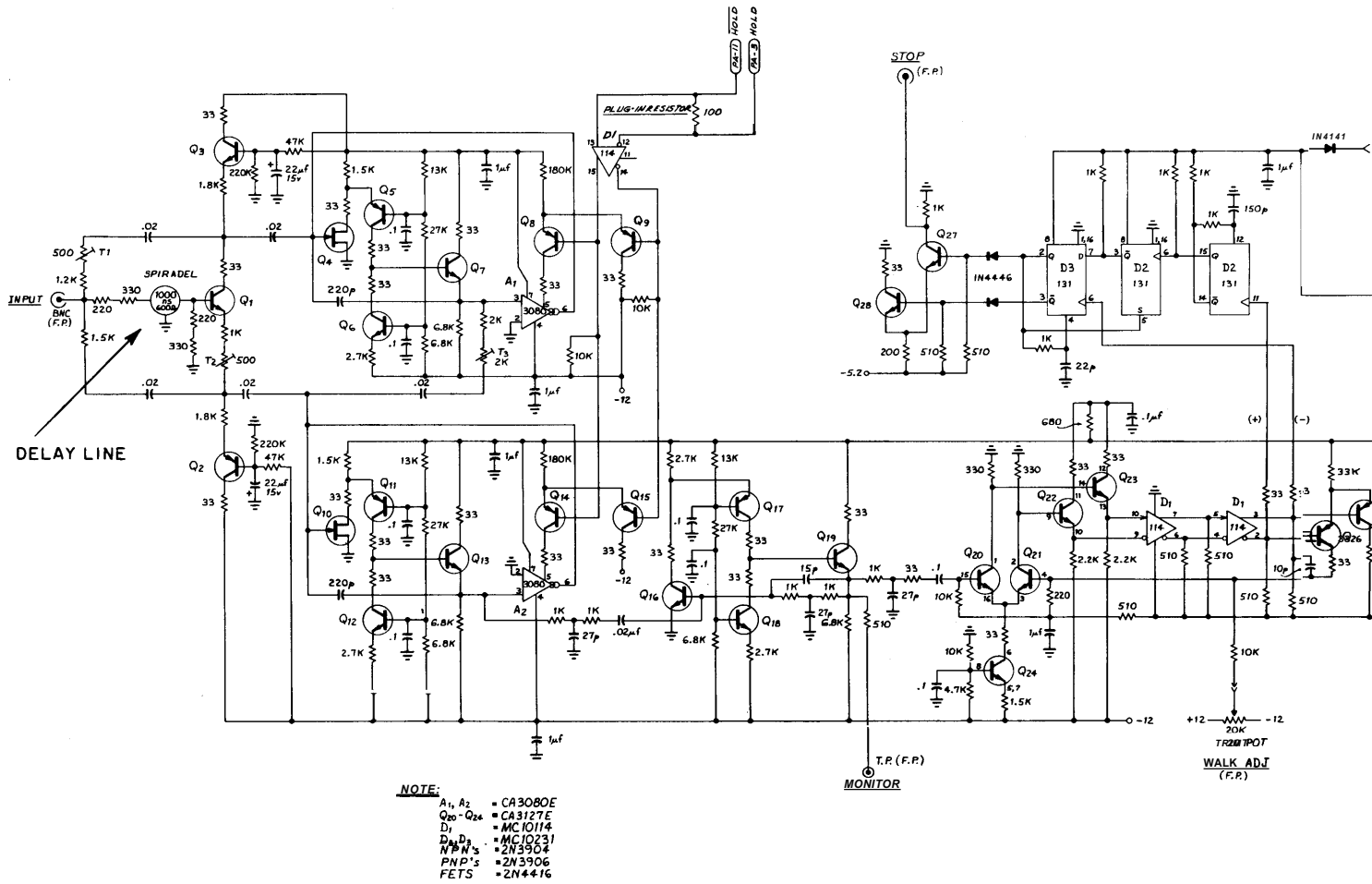


Fig. 13. Complete circuit diagram of the centroid finding filter and the zero crossing detector.

sample and hold circuit output level for each subdivision is the measure of the subdivided induced charge. These levels are sequentially switched into the centroid finding filter.

The details of the subdivision filter chain and multiplexer are described in ref. 3. The details of the centroid finding filter design are described here.

Fig. 12 illustrates a functional diagram of the centroid finding filter and the response at several nodes to an impulse input signal. The delay line, an inverting amplifier and an operational integrator (A, with feedback element C), are arranged to form a single delay line clipping and integration as is indicated by the impulse response shown at the output of A. The suitably weighted sum of A, output signal, the output signal of the delay line and the input signal, is integrated by the integrator circuit comprised of amplifier A, and feedback element C. The output of A, has the desired impulse response for centroid finding. The zero crossing time of the filter response is provided by the zero crossing detector circuit and is the measure of the centroid of the input signal. Transconductance amplifiers,  $G_1$  and  $G_2$ , connected in feedback of the integrator serve as restorers which are gated off during the filtering time,  $T_m$ . Fig. 13 shows the complete schematic diagram of the centroid finding filter.

Amplifier A, of the functional diagram is realized by a single pole amplifier with active elements  $Q_4$  through  $Q_7$ . The feedback elements are the 200 pF capacitor and the 3080 transconductance amplifier restorer. The restorer is gated off during the "hold" time of the subdivision sample and hold circuits. The inverting amplifier following the delay line is realized here with active

element  $Q_1$ . Amplifier A, of the functional diagram is formed similarly to A, and has active elements  $Q_{10}$  through  $Q_{13}$ . The response is smoothed by the filter-amplifier with active elements  $Q_{16}$  through  $Q_{19}$ .

Transistors  $Q_{20}$  and  $Q_{21}$  are the active differential input elements of the zero crossing discriminator detector. The current steering pair,  $Q_{25}$  and  $Q_{26}$ , provides the feedback for hysteresis. The current is quiescently flowing through  $Q_{26}$ , establishing the discriminator threshold level. When the discriminator fires, the current is steered through  $Q_{25}$  and the "0" threshold value is established. The following circuitry,  $D_1$ ,  $D_2$ , and output circuit with active elements  $Q_{27}$  and  $Q_{28}$ , provide a standardized output signal at the time the discriminator relaxes as the "0" threshold is crossed.

## References

- [1] J.L. Alberi, J. Fischer, V. Radeka, L.C. Rogers and B.P. Schoenborn, Nucl. Instr. and Meth. 127 (1975) 507.
- [2] V. Radeka and R.A. Boie, Nucl. Instr. and Meth. 178 (1980) 543.
- [3] R.A. Boie and V. Radeka, IEEE Trans. Nucl. Sci. NS-27 (1980) 338.
- [4] E. Gatti, A. Longoni, R.A. Boie and V. Radeka, Nucl. Instr. and Meth. 188 (1981) 327.
- [5] M.G. Strauss, R. Brenner, R.J. Lynch and C.B. Morgan, IEEE Trans. Nucl. Sci. NS-28 (1981) 800.
- [6] A.P. Jeavons, N.L. Ford, B. Lindberg and R. Sachot, IEEE Trans. Nucl. Sci. NS-25 (1978) 553.
- [7] G. Melchart, G. Charpak, F. Sauli, G. Petersen and J. Jacobe, Nucl. Instr. and Meth. 186 (1981) 613.